ORIGINAL ARTICLE

BDS and GPS side-lobe observation quality analysis and orbit determination with a GEO satellite onboard receiver

Wenwen Li[1] · Kecai Jiang[1] · Min Li[1,2] · Qile Zhao[1,2] · Meng Wang[3] · Chuang Shi[4] · Caijun Xu[5]

Abstract

Multi-GNSS combination can alleviate problems associated with GNSS-based geostationary earth orbit (GEO) satellite navigation and orbit determination (OD), such as GNSS availability and observation geometry deterioration. However, only GPS has been widely applied and investigated in GEO missions, whereas GEO OD with BDS requires further exploration. The Chinese GEO satellite TJS-5, equipped with a GPS and BDS-compatible receiver, is the first GEO mission that tracks both BDS 2nd and 3rd generation satellites since BDS global deployment. With the TJS-5 real onboard data, we evaluate BDS side-lobe signal performance and the BDS contribution to GEO OD. Due to transmit antenna gain deficiencies in the side lobes, BDS shows a worse tracking performance than GPS with an average satellite number of 4.3 versus 7.8. Both GPS and BDS reveal inconsistency between carrier-phase and code observations, which reaches several meters and significantly degrades post-dynamic OD calculation. We estimate the consistency as a random walk process in the carrier-phase observation model to reduce its impact. With inconsistency estimated, the post-fit carrier-phase residuals decrease from 0.21 to 0.09 m for both GPS and BDS. The OD precision is significantly improved, from 1.95 to 1.42 m with only GPS and from 3.14 to 2.71 m with only BDS; the GPS and BDS combined OD exhibits the largest improvement from 1.74 to 0.82 m, demonstrating that adding BDS improves the OD precision by 43.3%. The above results indicate that the proposed carrier-phase inconsistency estimation approach is effective for both GPS and BDS and can achieve an orbit precision within 1.0 m using multi-GNSS measurements.

Keywords BDS · Geostationary earth orbit · Side-lobe signal · Observation quality · Carrier-code inconsistency · Orbit determination · Orbit precision

Introduction

High and geostationary earth orbit (HEO/GEO) satellites are widely used for earth observation, weather forecasting, global communication, etc., which require onboard

✉ Kecai Jiang
kc.jiang@whu.edu.cn

[1] GNSS Research Center, Wuhan University, 129 Luoyu Road, Wuhan 430079, China

[2] Collaborative Innovation Center of Geospatial Technology, 129 Luoyu Road, Wuhan 430079, China

[3] Beijing Institute of Satellite Information Engineering, Beijing 100095, China

[4] School of Electronic and Information Engineering, Beihang University, 37 Xueyuan Road, Beijing 100191, China

[5] School of Geodesy and Geomatics, Wuhan University, 129 Luoyu Road, Wuhan 430079, China

or post-processed orbital precision ranging from several kilometers to even submeter levels (Huang et al. 2009; Nicolás-Álvarez et al. 2019; Ramsey et al. 2019; Winternitz et al. 2017). In recent years, a growing number of HEO/GEO satellites have been equipped with space-borne global navigation satellite system (GNSS) receivers for onboard navigation (Ashman et al. 2018; Enderle et al. 2018). For HEO/GEO missions, only the GNSS signals from the Earth's opposite side can be tracked, which are primarily side-lobe signals. This results in lower received signal power, larger observational error, fewer visible satellites, and poorer observation geometry than ground applications (Bauer et al. 2017; Lin et al. 2020). To better support HEO/GEO navigation, dedicated efforts have been undertaken on satellite signal characterization and modernization as well as high-sensitivity receiver development (Marquis and Reigh 2015; Ramsey et al. 2019; Wang et al. 2022).

The conception of space service volume (SSV) is established to describe GNSS service performances for space applications that extend from 3000 to 36,000 km above the earth's surface (the geostationary orbit altitude) (Bauer et al. 2006). Considering multi-GNSS development in recent decades, the initiative of developing an interoperable multi-GNSS SSV among each GNSS provider has been promoted (Bauer et al. 2017; United Nations Office for Outer Space Affairs 2018). Nevertheless, official SSV specifications consider only main-lobe signals and neglect the extensive side-lobe signals, severely underestimating GNSS signal availability for HEO/GEO navigation (Lin et al. 2020; Parker et al. 2016). To assess GPS side-lobe signal quality and facilitate GPS for GEO/HEO applications, Lockheed Martin released the detailed GPS antenna gain patterns obtained from factory tests (Marquis and Reigh 2015). The GPS antenna characterization experiment (ACE), a research collaboration between Aerospace Corporation and NASA Goddard Space Flight Center (GSFC), comprehensively characterized on-orbit GPS transmit antennas using numerous GEO onboard observations (Donaldson et al. 2020). The ACE results reveal new knowledge of side-lobe signal patterns and indicate that the quality of side-lobe signals can meet the requirement for HEO/GEO navigation.

The benefits of side-lobe signals in HEO/GEO navigation have already been demonstrated in various space applications, such as the geostationary operational environmental satellite-R program (GOES R) (Chapel et al. 2017; Ramsey et al. 2019; Winkler et al. 2017). Different from main-lobe signals, the side-lobe signals present biases reaching up to several meters based on the real onboard data. The ACE datasets indicate that side-lobe observation biases remain consistent at different signal levels (Donaldson et al. 2020). In GOES R-17 OD calculations, these biases are represented as highly variable elevation-dependent variations in the post-fit pseudorange residuals, which are thought to be caused by variations of the L1 frequency signal group delay between the side lobe and the edge of the main lobe (Winkler et al. 2017). The post-fit carrier-phase residuals from dynamic OD of Chang'e-5T and TJS-2 satellites also indicate large linear trends and are presumably attributed to ionospheric refractions (Jiang et al. 2018; Su et al. 2017). Though the definitive cause of such biases is still unknown, different approaches are proposed to handle them. Winkler et al. (2017) estimated one bias for each GPS observation arc, which reduced the GOES R-17 code residuals from 2.06 to 0.23 m. Considering that TJS-2 post-fit residuals exhibited a daily repetitive pattern due to satellite geometry, Jiang et al. (2018) built a sidereal filter to correct such errors,

which reduced TJS-2 orbit overlap differences (OODs) from 2.14 to 0.99 m.

Combining multiple GNSSs can significantly improve observation geometry for GEO/HEO satellites. However, new emerging GNSS systems, such as BDS, still lack investigations. The two Chinese GEO satellites, i.e., No.2 and No.5 telecommunication technology test satellites (TJS-2 and TJS-5), are equipped with multi-GNSS receivers that can simultaneously track GPS, BDS, and GLONASS. For TJS-2, the navigation precision with only GPS is about 41.4 m; it is improved to 40.0 m and 16.9 m when GLONASS and BDS satellites are added, respectively, though their average satellite numbers are only 4.6 and 0.8 (Wang et al. 2021a). The receiver on TJS-5 is BDS 2nd (BDS-2) and 3rd generation (BDS-3) compatible, allowing investigations on the BDS performances using the complete BDS constellation. Wang et al. (2022) evaluated the in-orbit signal quality of BDS-3 satellites and reconstructed the BDS transmit antenna gain patterns with the TJS-5 measurements, indicating a degraded performance of BDS-3 side-lobe signals. When BDS is incorporated, the TJS-5 navigation precision improves significantly from 32.1 m to 16.5 m, which is consistent with TJS-2 results (Wang et al. 2021b). However, the above studies are limited to the GEO navigation performance evaluation with BDS involved, not considering the post OD.

This study focuses on the performance of TJS-5 navigation and post OD with BDS as well as GPS and BDS combination. TJS-5 onboard GPS and BDS side-lobe signal quality is firstly assessed, which reveals significant inconsistency between code and carrier-phase. An adjusted carrier-phase model is thus established to estimate such inconsistencies during OD. With the adjusted model, post-OD for TJS-5 is conducted with different GNSSs and the corresponding OD precision is compared. The following is the structure of this paper: In Sect. 2, the TJS-5 satellite and the data used in this study are described; in Sect. 3, the TJS-5 onboard GPS and BDS data quality analysis are presented in terms of satellite visibility, carrier-to-noise ratio (CNR) variations as well as observation errors; the post OD performance using GPS and BDS is evaluated in Sect. 4; at last, Sect. 5 gives the conclusions.

TJS-5 satellite description and data collection

The TJS-5 satellite, launched on January 7, 2020, is located at a geostationary orbit around 178.5° E. As a follow-on mission of TJS-2, TJS-5 also carries a set of GNSS receivers and a high-gain antenna for onboard

Fig. 1 Schematic diagram of TJS-5 receiving side-lobe signals for navigation. The gray and red shades indicate the main-lobe and side-lobe signal ranges, respectively. The signal lobes of BDS GEO/IGSO and GPS satellites are zoomed out for a clear view
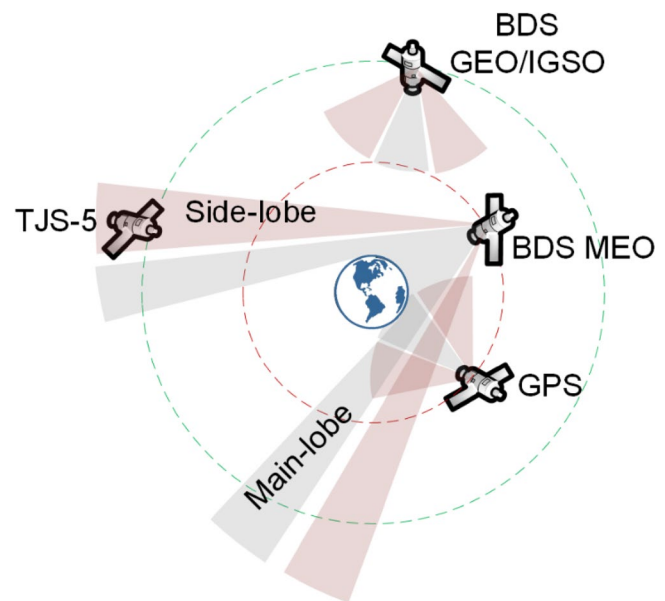
navigation. To track both main- and side-lobe signals transmitted by GPS and BDS satellites on the opposite side, the TJS-5 onboard antenna is installed to point toward the center of earth, as illustrated in Fig. 1. The receiver is upgraded based on the one equipped by TJS-2 with several improvements. Firstly, the channel number and channel allocation strategy are changed. There are two modules in TJS-2's receiver, each with 16-channel hardware correlators. One module allocates 8 channels for GPS satellites and 8 for BDS, while the other 8 for GPS and 8 for GLONASS; however, they could not work simultaneously (Wang et al. 2021a). The receiver onboard TJS-5 has 24 channels equally allocated for tracking the BDS, GPS, and GLONASS signals, respectively. Such an update is reasonable as more satellites could be tracked simultaneously. Secondly, the newly launched BDS-3 satellites could also be tracked by TJS-5 in addition to legacy BDS-2 satellites, which provides a valuable source for evaluating the BDS-3 performance.

The onboard receiver can track three frequency signals, explicitly the GPS L1C, BDS B1I, and GLONASS L1; however, only the BDS and GPS measurements are streamed back to the ground for post-analysis. The BDS and GPS data from May 19 to 24, 2020, are provided by Space Star Technology Co., Ltd (TJS-2/5 satellite and onboard receiver manufacturer). These data are in an interval of 2 s and include observations of pseudorange, carrier-phase, and CNR. The final multi-GNSS precise orbit and clock (in an interval of 30 s) products generated at Wuhan University are collected to perform TJS-5 OD analysis (Zhao et al. 2022). The final orbit and clock products reach precisions at a few cm, far exceeding the OD precision that could be expected for a GEO-based receiver.

TJS-5 onboard GPS/BDS data quality analysis

In addition to GPS, TJS-5 provides an opportunity for investigating the real side-lobe BDS signals. The GPS and BDS data quality are evaluated in terms of satellite visibility, CNR variation, observational noise, and inconsistency errors.

Satellite visibility

Reception of the weak side-lobe GNSS signal is one of the main challenges for GNSS-based GEO navigation, thus making satellite visibility a critical indicator of data quality. Figure 2 illustrates the GPS and BDS satellite footprints in the local orbital frame. The azimuth is measured from the TJS-5 satellite flight direction pointing toward the geographical east direction, while the off-boresight from the radial. Two subplots are generated for the BDS satellites; one includes BDS-2 GEOs and IGSOs of higher orbit altitudes, while the other consists of the BDS-2 and BDS-3 medium earth orbit satellites (MEOs).

The GPS and BDS satellites are symmetrically distributed along the velocity direction. The off-boresight angles of GPS and BDS MEOs are mainly confined between 13° and 40°. BDS-2 MEOs are tracked with a wider azimuthal range than GPS and BDS-3 MEOs when the off-boresight is around 40°, mainly attributed to the back-lobe signals that are transmitted from the satellite back-side with a nadir exceeding 90° (Wang et al. 2022). BDS-2 GEOs and IGSOs are tracked within the aft hemisphere as they are geographically on the west side of TJS-5. The off-boresight angles of BDS-2 GEOs and IGSOs are approximately around 80° and 60°, respectively, which are both far beyond the TJS-5

Fig. 2 Sky view of GPS and BDS satellites in TJS-5 antenna reference fame. Top panel: GPS satellites; middle panel: BDS-2 and BDS-3 MEO satellites; bottom panel: BDS-2 GEO and BDS-2 IGSO satellites ▶

antenna beam range. Such exceptions are made by receiver gain designs to improve the observation geometry.

Figure 3 illustrates the frequency count of the GPS and BDS visible satellite number per epoch as observed by TJS-5. The visible GPS satellite number is mostly over 6; it stays at 8 for about 86% epochs up to its full channel limitation. However, such performance is uncompetitive compared to other GEO missions, e.g., GOES R-16 and R-17 satellites can track 12 GPS satellites for most epochs (Chapel et al. 2017; Ramsey et al. 2019). TJS-5 onboard receiver tracks BDS satellites with a PRN number below C37 in its current firmware state. Though the channel number allocated for BDS satellites is the same as GPS, the actual observed BDS satellite number is much fewer. There are about 32% epochs with less than 4 BDS satellites, which undermines the onboard navigation continuity with independent BDS system. Considering the whole 5-day observation arc, the average GPS satellite number is about 7.8 while BDS is 4.3, resulting in a sum of about 12.1.

CNR variations

The highly dynamic CNR fluctuations from a GEO-based receiver reveal unique GNSS transmit antenna patterns which are associated with satellite block types (Chapel et al. 2015; Donaldson et al. 2020). Thus, CNR variations are assessed with different satellite types in Fig. 4, explicitly the GPS Block IIR-A, IIR-B, IIR-M, IIF, IIIA, as well as BDS-2 IGSO, BDS-2 MEO, and BDS-3 MEO. Their averaged CNR values are calculated in 1° nadir bins and depicted in Fig. 5; the BDS-2 GEOs are not shown as they are in a static geometry relative to TJS-5. The BDS-3 MEO satellites are divided into two groups according to their manufacturers: CAST (China Academy of Space Technology) and SECM (Shanghai Engineering Center for Microsatellites).

The GPS side-lobe signals could be tracked to nadirs around 80° and for Block IIR-A even to 100°. According to the averaged CNR series, the Block IIR-A satellites reveal a narrower main beam width but a higher CNR level than other GPS Block types, which is because the Block IIR-A satellites are of higher transmit power and do not suppress the side-lobe signal powers as the other Blocks do (Marquis and Reigh 2015; Parker et al. 2016). Both Block IIF and IIIA satellites indicate null zones in low gain regions around nadirs of 43° and 60°, respectively. The averaged CNR series of Block IIIA show similar variations with respect to Block IIR-B and IIR-M.
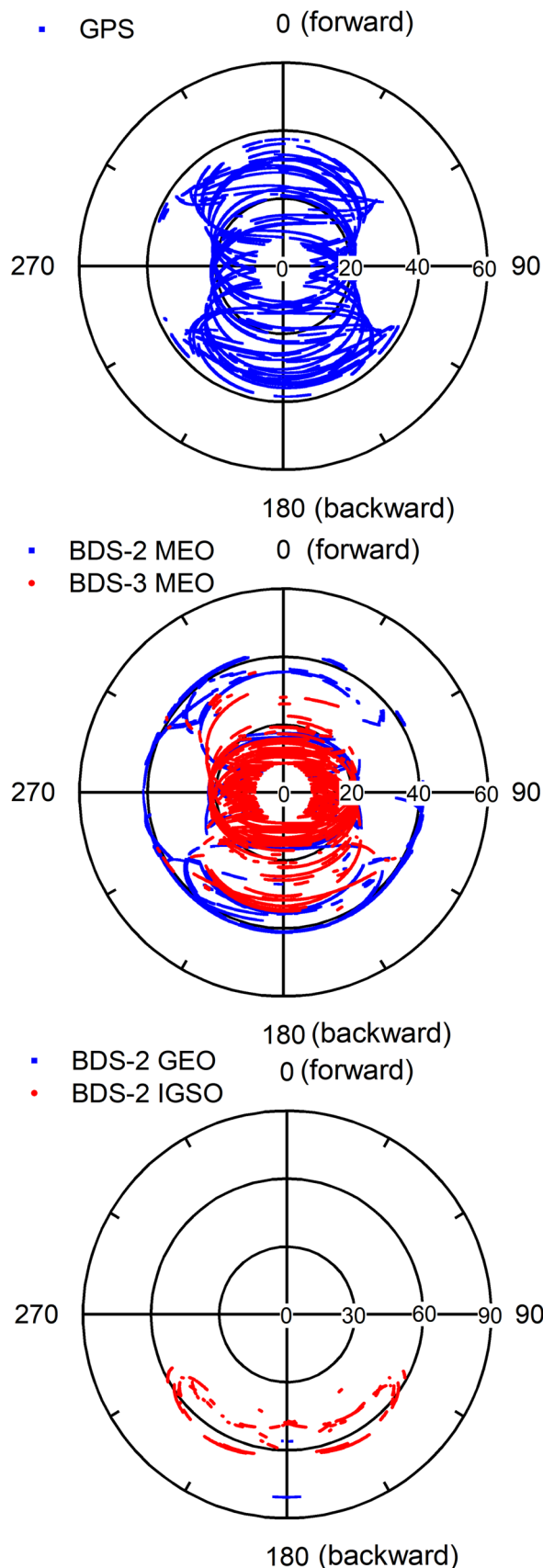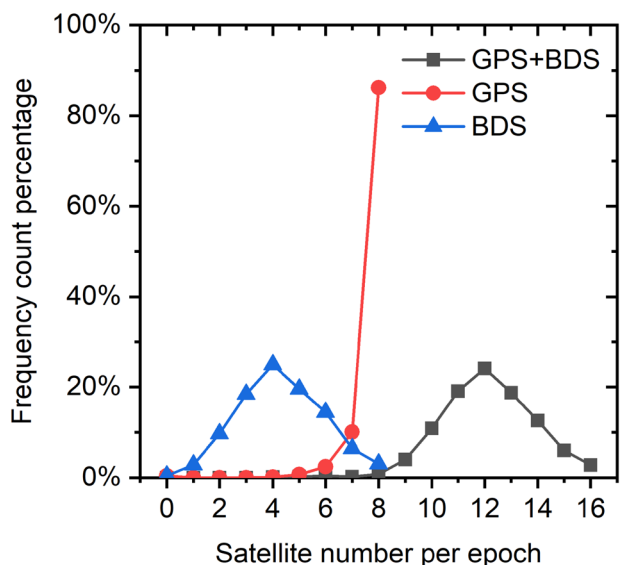
Fig. 3 Frequency count of GPS and BDS satellite number per each epoch. The average satellite number for GPS and BDS is 7.8 and 4.3, respectively. The fewer BDS number is due to degraded BDS side-lobe signal gains

The CNR variations of BDS satellites exhibit very distinct patterns from one satellite type to another. BDS IGSOs signals are only available from side lobes with a CNR of 25–40 dB-Hz and a nadir range of 45° to 65° due to geometric limits. The BDS-2 MEOs signals can be tracked to nadirs even beyond 120° and show strong signal powers in the side and back lobes; the peak CNR is 45 dB-Hz, nearly 10 dB-Hz higher than other types. The two BDS-3 MEOs types show coincident CNR decrement as the nadir approaches 40°. The BDS-3 MEO (CAST) signals exhibit rapid CNR decrement as nadir increases from 40° to 50° and show unstable tracking for nadirs over 50°, indicating possible side-lobe signal suppression when the nadir grows over 40°. Comparatively, the CNR scatters of BDS-3 MEO (SECM) range from 25 to 40 dB-Hz and reveal a much wider side-lobe beam, with nadirs even reaching 80°. According to the averaged CNR series, BDS-2 MEOs main-lobe signals present a beam width about 5° narrower than BDS-3 MEOs. Due to decreased signal transmission power, the main-lobe peak CNR of BDS-2 MEOs is 47 dB-Hz, about 3 dB-Hz lower than BDS-3 MEOs; however, the CNR in side lobes reaches the maximum of 38 dB-Hz at a nadir around 70°, about 8 dB-Hz higher. The averaged side-lobe CNR of BDS-3 MEO (SECM) stays around 30 dB-Hz, while that of BDS-3 MEO (CAST) exhibit a significant reduction from 32 dB-Hz to 25 dB-Hz, indicating that the side-lobe signal performance of BDS-3 MEO (SECM) is much better than BDS-3 MEO (CAST).

Fig. 4 GPS and BDS satellite CNR against nadir angles. Different panels denote different satellite types. The BDS-2 GEO satellites are not shown as their nadirs nearly stay fixed. The BDS-3 satellites indicate degraded CNR levels compared to other types, especially the BDS-3 MEO (CAST)
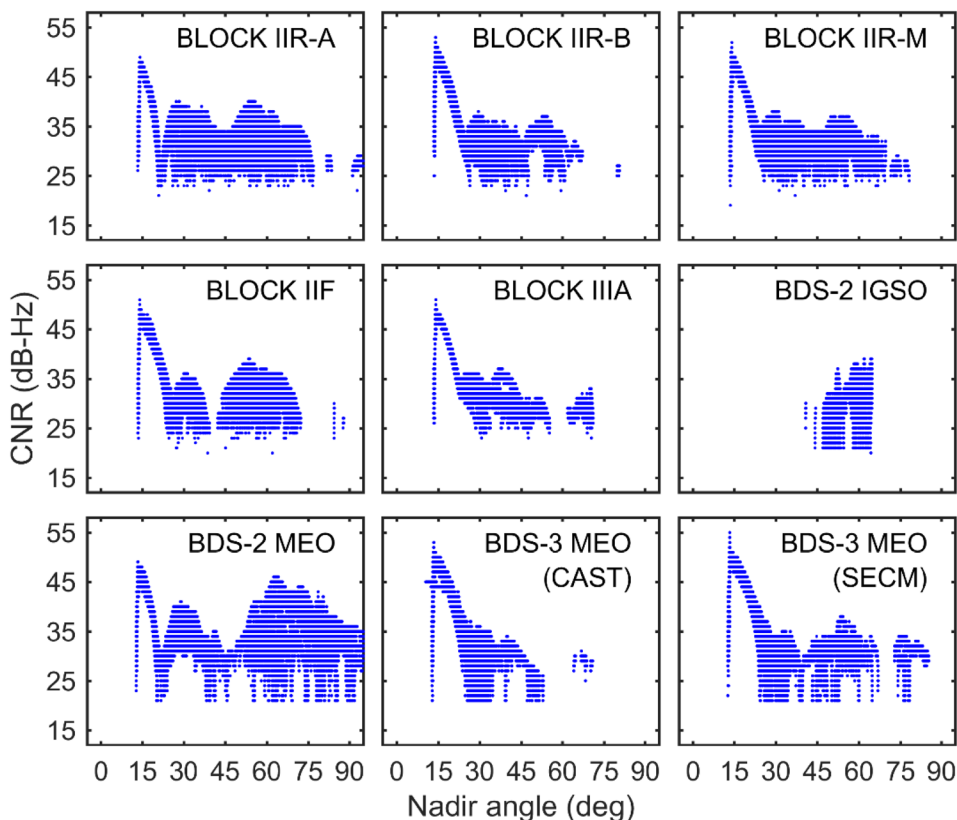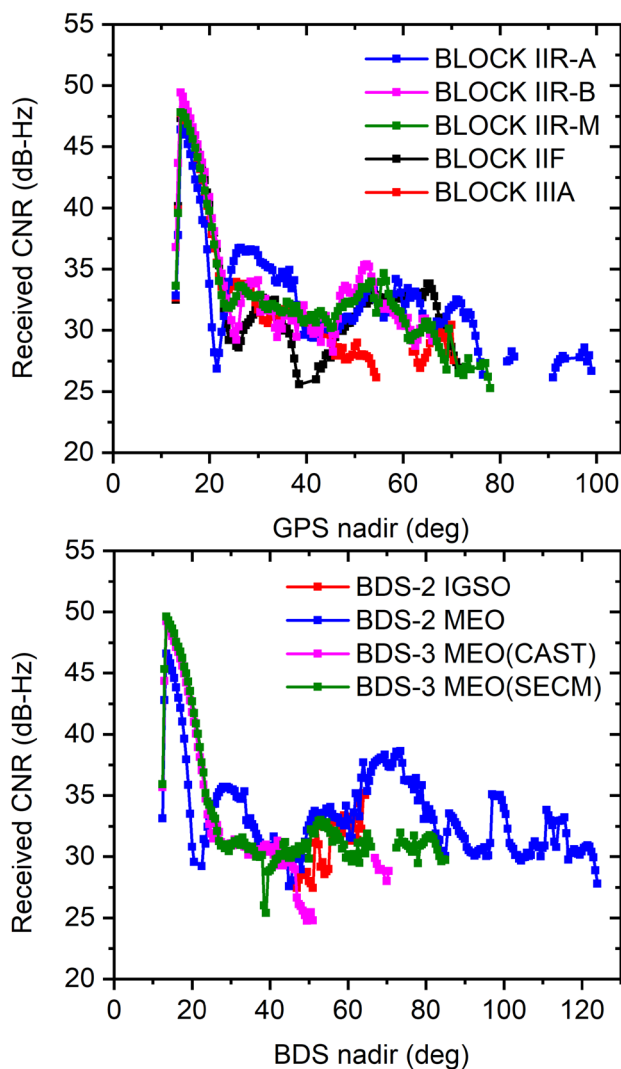
Fig. 5 GPS (top panel) and BDS (bottom panel) averaged CNR variations against nadir angles in 1° bins. Different colors denote different satellite types

Code and carrier-phase noise and inconsistency evaluation

The between-epoch triple differencing approach, which is a representation of the observation third derivatives by epoch difference arithmetic, is used to evaluate high-frequency observation noise (Jiang et al. 2018; Li and Geng 2019), while the carrier-code geometry-free combination method is employed to analyze carrier-code inconsistency. It is worth noting that the raw carrier-code differences derived from the geometry-free combination mainly indicate the code observation errors; to represent carrier-code inconsistencies, the high-frequency code noise presented in the difference series should be firstly filtered out. The code and carrier-phase triple differences as well as the carrier-code differences are displayed in Fig. 6 along with GPS or BDS nadir angles

and the CNR variations. The carrier-code inconsistencies are also shown by smoothing the carrier-code differences using a moving averaging filter. Three satellites are selected for the illustration, explicitly G20 (Block IIR-A), C12 (BDS-2 MEO), and C33 (BDS-3 MEO). Due to possible corruption of ionospheric refraction, observations are discarded if their nadirs are within 17.5° (corresponding to 2000 km above earth surface) (Li et al. 2019).

The subplots of G20 demonstrate typical GPS side-lobe signal signatures. The triple differences of both code and carrier-phase indicate consistent variations to CNR, and their fluctuation magnitudes are similar compared to the TJS-2 results (Jiang et al. 2018). Particularly, the carrier-code inconsistencies indicate systematic changes reaching several meters, especially at the edges between different side lobes.

Different features of BDS side-lobe signals are revealed by C12 and C33. The C12 nadir increases from 54° to 105° during the selected period, indicating both side- and back-lobe signals. When its nadir is between 60° and 70°, the CNR fluctuates dynamically with a variation amplitude of 25 dB-Hz and present multiple interruptions, indicating the signal powers are unstable within this side-lobe range. When nadir increases above 70°, C12 can be again tracked continuously with a relatively high CNR level decreasing from 40 to 30 dB-Hz, and the variations of code triple differences are reduced from ± 15 m to less than ± 5 m. The C12 phase triple differences are mainly between ± 0.2 cycles, and the carrier-code differences exhibit few systematic variations. The C33 nadir stays between 17.5° and 26.0° and the CNR varies between 25 and 50 dB-Hz, indicating signals across the main lobe and the first side lobe. Due to a higher CNR level, C33 triple differences show much smaller variations than G20 and C12, varying within ± 4 m and ± 0.2 cycles for code and phase, respectively. The C33 carrier-code differences show strong correlations with nadir and CNR and exhibit significant systematic changes about 3–4 m, indicating the carrier-code inconsistencies.

According to TJS-5, the carrier-code inconsistencies are found valid for both GPS and BDS data, and are mainly at the edges between different lobes. Particularly, the inconsistencies at lower nadirs, i.e., between main and side lobes, present larger variations, which might be mostly due to topside ionosphere refractions as shown in Jiang et al. (2018) and Li et al. (2019); however, for high nadirs, the main cause might be attributed to the hardware delay variations between different lobes, which is indicated by the GOES R-17 results as well (Winkler et al. 2017).

The root mean squares (RMS) values of the triple differences and the carrier-code differences are calculated against CNR in 1 dB-Hz steps, as shown in Fig. 7. Generally, the carrier-phase noise of BDS and GPS are at similar levels whereas the BDS code noise is overall superior to
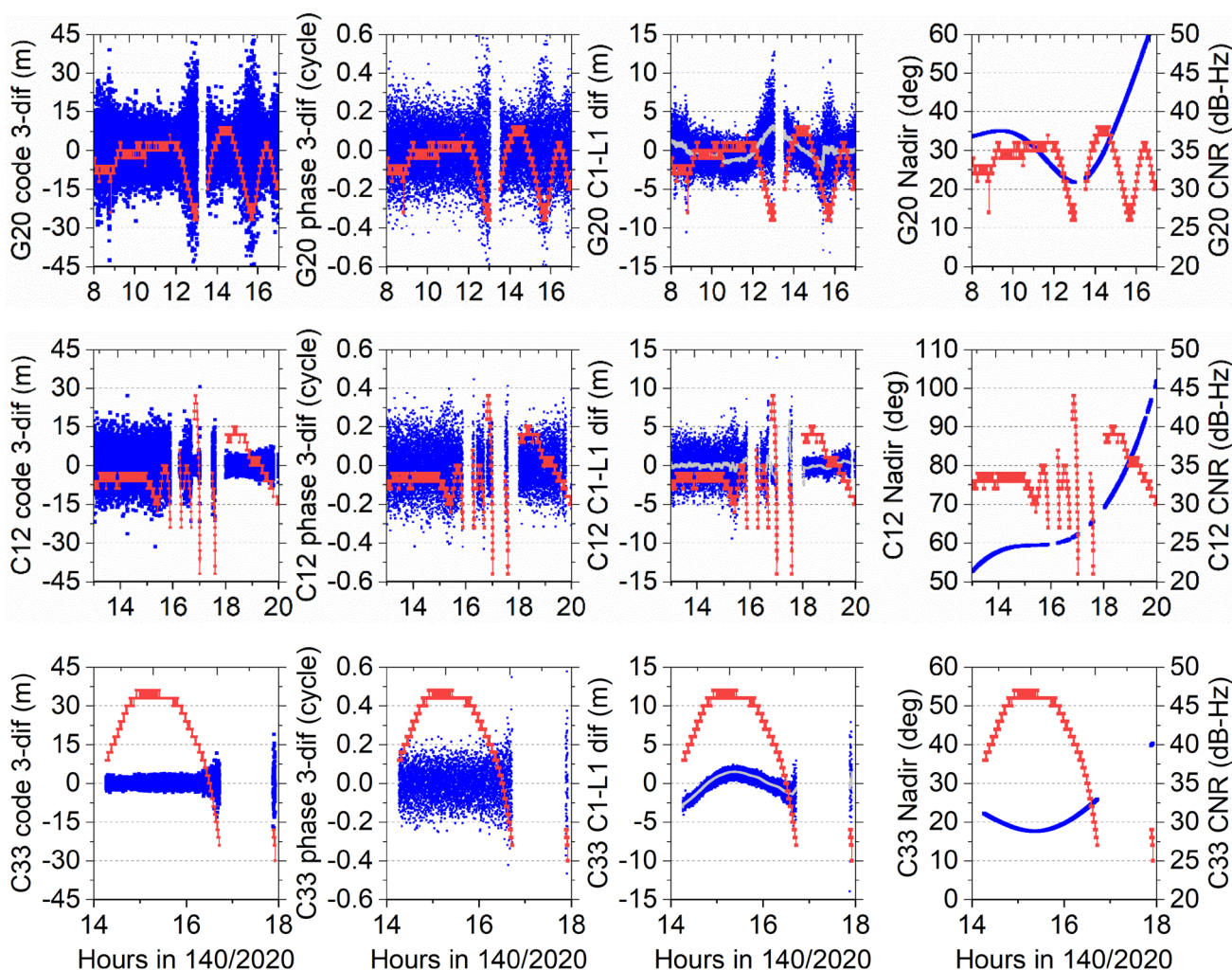
Fig. 6 Observation precision analysis for different satellites including G20 (top panel), C12 (middle row), and C33 (bottom panel). First column: the code triple differences; second column: the carrier-phase triple differences; third column: carrier-code differences; last column: nadir angles. The CNR series are plotted in red lines in each panel for evaluating the correlations. The gray lines in the third column panels represent the smoothed carrier-code differences by a moving averaging filter

GPS; they all exhibit significant decrement as CNR grows. Regardless of their satellite types, the carrier-phase triple differences decrease from 0.35 cycles to 0.10 cycles when CNR increases from 25 to 50 dB-Hz, while the GPS and BDS code triple differences decrease from 20 to 3 m and from 15 to 3 m, respectively. The GPS and BDS carrier-code differences mainly represent code observation errors, revealing similar decremental trends as the code triple differences but with a smaller magnitude from about 4 m to 1 m, due to that the noise derived from triple differencing is magnified by $\sqrt{20}$ (Li and Geng 2019). For GPS and BDS, the overall average RMS values of carrier-phase triple differences are 0.14 cycles and 0.11 cycles, respectively, while code triple differences are 10.0 m and 5.3 m, as well as carrier-code differences 1.65 m and 1.74 m, respectively.

TJS-5 dynamic orbit determination analysis

TJS-5 dynamic OD is conducted in this section utilizing both code and carrier-phase observations. A new carrier-phase observation model is proposed to account for the carrier-code inconsistency. The OD performance is then investigated with different GNSS system observations.

Orbit determination strategy

The arc length for TJS-5 OD is set to 30 h, starting at 21:00 the previous day and ending at 03:00 the next. Thus, 6-h overlap orbit differences (OODs) between adjacent arcs could be calculated for OD precision analysis. Table 1 lists the detailed OD strategy, including satellite dynamic models and observation models. Gravitational perturbations are

Fig. 7 Statistics of observation precisions of different BDS and ▶
GPS satellite types. The RMS values are calculated in 1 dB-Hz bins
against CNR. Blue lines and dots represent BDS while red GPS. Top
panel: RMS of code triple differences; middle panel: RMS of carrier-
phase triple differences; bottom panel: RMS of carrier-code differ-
ences

calculated using empirical models with sufficient accuracy,
i.e., EIGEN-06C (Foerste et al. 2011) for static earth gravity
and FES 2004 (Lyard et al. 2006) for ocean tide perturba-
tions. However, non-gravitational perturbations for TJS-5
remain large uncertainties, among which the solar radiation
pressure (SRP) is regarded as the main problem. Employed
extensively in GNSS satellite OD, the ECOM (extended
CODE orbit model) SRP model can be flexibly adjusted
for satellites of different orbit types and attitude regimes
(Arnold et al. 2015) and is thus incorporated for TJS-5 OD.
For observation models, the multi-GNSS precise ephemeris
and clock offset products released by Wuhan University are
utilized. Observations of nadirs within 17.5° are discarded
due to probable ionospheric refractions.

Estimation of carrier-code inconsistencies

The carrier-code inconsistency errors represented as sys-
tematic trends in post-fit carrier-phase residuals are hard
to eliminate. Jiang et al. (2018) proposed the sidereal filter
method to correct such errors considering the daily repeat-
able pattern. However, since there are frequent interruptions
during tracking BDS satellites, it is difficult to construct a
sidereal filter that can provide proper corrections to all the
BDS observations.

   To correct these inconsistency errors, we adjust the clas-
sic carrier-phase model by estimating them. For each GNSS
satellite, the carrier-phase observation equation is inserted
with an inconsistency parameter which is parameterized as a
random walk process noise. This yields the proposed carrier-
phase along with the code observation models as expressed
below:

$$
\begin{aligned}
L_{i.S} &= R_i + c\left(t_{r,S} - t^i\right) + \lambda_i N_i + X_i + \Delta_{L,i} + \varepsilon_{L,i} \\
P_{i.S} &= R_i + c\left(t_{r,S} - t^i\right) + \Delta_{P,i} + \varepsilon_{P,i}
\end{aligned}
\tag{1}
$$

where i denotes for a specific GNSS satellite and S for its
system; P, L and R are the pseudorange, carrier-phase obser-
vations and the geometric distance, respectively; $t_{r,S}$ and t^i
refer to the receiver and the GNSS satellite clock offsets,
respectively; note that different receiver offsets are estimated
for different systems epoch-wisely; λ_i and N_i are the wave-
length and ambiguity, respectively; X_i refers to the carrier-
code inconsistency parameter modeled as random walk
process noise; $\Delta_{P,i}$ and $\Delta_{L,i}$ denote all other errors associ-
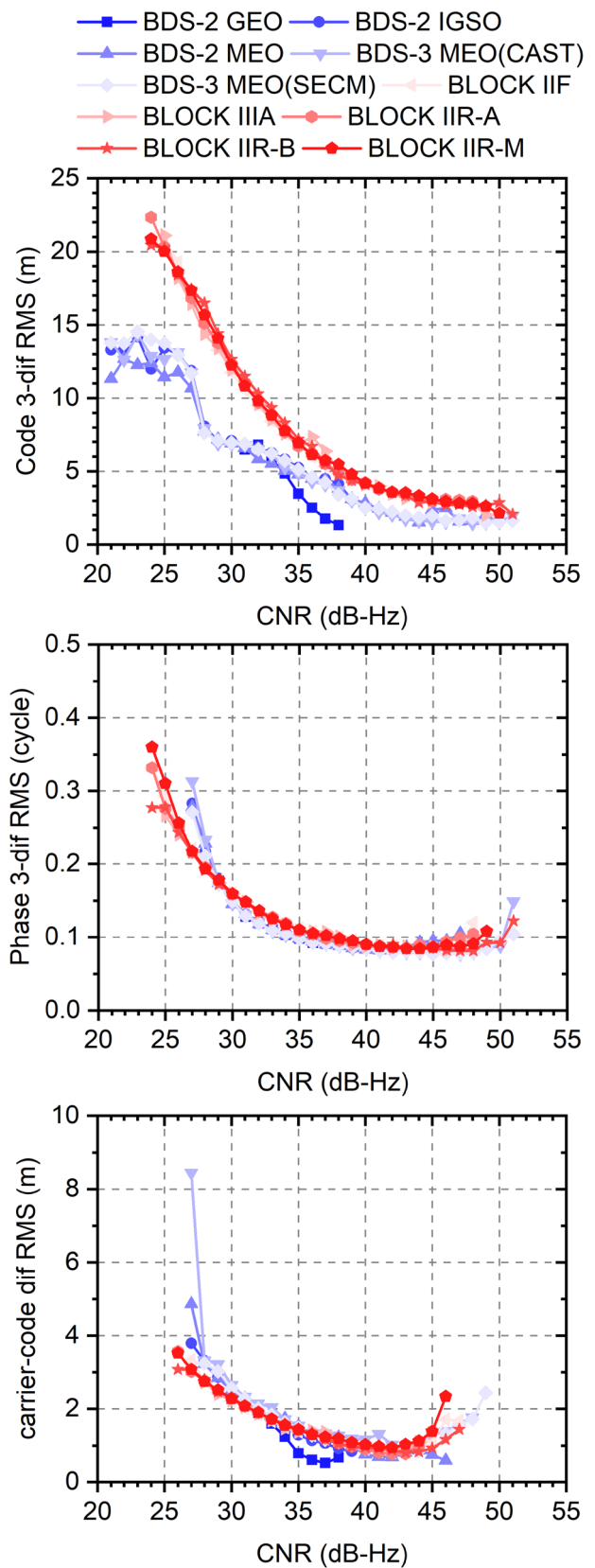ated with code and carrier-phase observations, respectively,

Table 1 TJS-5 orbit determination strategy

Orbit models	
Reference frame	International celestial reference frame
Earth orientation	IERS earth orientation parameters 14 C04 solution (Bizouard et al. 2019)
Gravity model	EIGEN-06C, 12X12 degree and order (Foerste et al. 2011)
Solid earth tide and pole tide	IERS Conventions 2010 (Petit et al. 2010)
Ocean tide	FES 2004 (Lyard et al. 2006)
N-body perturbation	JPL DE405
Relativity	IERS Conventions 2010 (Petit et al. 2010)
SRP	ECOM model (Arnold et al. 2015; Wang et al. 2019)
Observation models	
Observations	GPS: C1C, L1C; BDS: B2I, L2I
Arc length and sampling interval	30 h and 30 s
Observation mask	17.5° of GPS/BDS nadir angle
GPS and BDS orbit and clock	precise orbit products from Wuhan University
GPS and BDS antenna PCO and PCV	IGS ATX model (igs14 file) (Rebischung and Schmid 2016)
TJS-5 antenna phase center	PCO from manufacturer; PCV ignored
Relativistic effects	IERS Conventions 2010 (Petit et al. 2010)
Atmospheric refractions	Ignored
Estimated parameters	
TJS-5 initial state	Position and velocity at initial epoch
Dynamic parameters	All 9 parameters of ECOM model
Receiver clock offsets	One per each epoch as white noise process
Ambiguities	One per each continuous satellite pass

i.e., relativistic delay, antenna phase center offsets as well as phase windup errors; $\varepsilon_{P,i}$ and $\varepsilon_{L,i}$ are the code and carrier-phase noise, respectively.

Constraints on the carrier-code inconsistency parameters are crucial during estimation. Since the inconsistency and the ambiguity parameters are highly correlated, the inconsistency parameters degrade the weights of carrier-phase observations if a loose constraint is assigned; on the other hand, they may be absorbed into ambiguity estimates if the constraint is too strong. Thus, a proper process noise should be determined.

GPS data from DOY 140–144, 2020 are utilized for analyzing the constraints on carrier-code inconsistencies. Different process noise is assigned during OD, explicitly 0.0001, 0.0005, 0.001, 0.002, and 0.004 m/$\sqrt{\Delta t}$, where Δt is the processing interval of 30 s. As a typical illustration, the inconsistency estimates and the carrier-phase residuals of G20 are displayed in Fig. 8 along with the carrier-code differences after low-pass filtering for comparison. With a constraint of 0.0001 m/$\sqrt{\Delta t}$, the carrier-phase residuals exhibit similar variations of ± 1.0 m compared to the filtered carrier-code differences whereas the estimated inconsistencies are mostly around zero. This indicates that the carrier-code inconsistencies are the main error source degrading carrier-phase model. As the process noise increases, the post-fit residuals decrease dramatically while the inconsistency
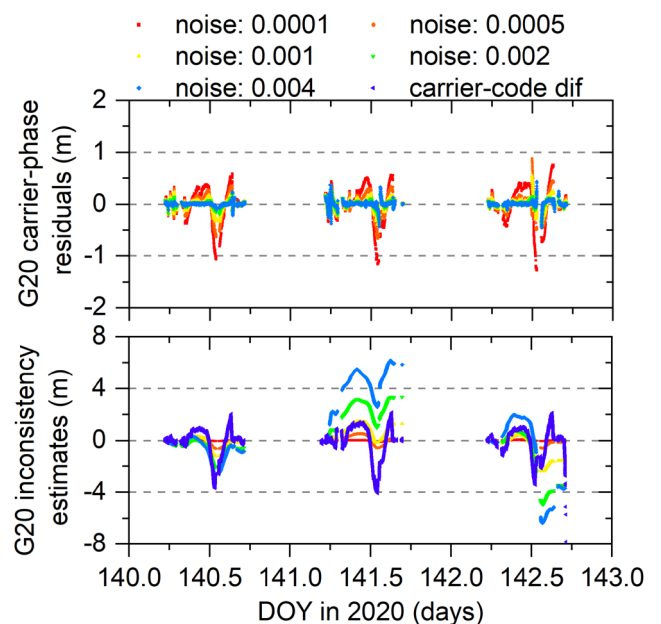

Fig. 8 G20 carrier-phase residuals (top panel) and carrier-code inconsistency estimates (bottom panel) during DOY 140-142/2020. Different colors represent different process noise values assigned to the inconsistency parameter. The filtered carrier-code differences are shown in the bottom panel

estimates fluctuate more closely to the carrier-code differences, indicating that the adjusted carrier-phase model can effectively represent the carrier-code systematic differences and improve carrier-phase function model. Specifically, when the process noise increases to above 0.001 m/$\sqrt{\Delta t}$, the residuals reduce to about ± 0.2 m and the tendency variations are significantly mitigated, while inconsistency estimates reveal variations about a few meters and show similar trends comparing to the carrier-code differences. The inconsistency estimates show noticeable offsets between different blocks reaching several meters, which are mainly attributed to the strong correlations between the inconsistency and ambiguity parameters, and can be mostly compensated by ambiguities during estimation. It is also worth noting that both the inconsistency estimates and the carrier-code differences exhibit daily repetitive signatures, which is in accord with the results in Jiang et al. (2018) and confirms the effectiveness of the proposed carrier-phase model.

All the carrier-phase residuals at different process noise levels are illustrated against epochs as well as GPS nadirs in Fig. 9. Systematic trends could be observed, which indicates larger variations with lower nadirs. The residuals reach about ± 1.0 m at the lowest nadirs of 17.5° and ± 0.05 m at around 75°. As the process noise increases, the systematic variations are significantly reduced. Especially when

the process noise is set to 0.004 m/$\sqrt{\Delta t}$, the overall phase residuals fall between ± 0.2 m.

The orbit consistency is evaluated by OODs. The RMS values of OODs in the along-track, cross-track, and radial components are displayed in Fig. 10. For comparison, the baseline OD solution is also performed using the conventional carrier-phase model. All OD solutions show precisions generally at 1–2 m level in the three components. When the process noise is 0.0001 m/$\sqrt{\Delta t}$, the orbit precision is comparable to the baseline solution, indicating a tight constraint. When the process noise increases, the errors in the radial component reveal a pronounced decrement from around 1.3 m to 0.5 m level. However, the other two components present more complicated behaviors; generally, their RMS values firstly reduce and then increase as the process noise grows. When the process noise is within 0.0005–0.002 m/$\sqrt{\Delta t}$, improvements can be obtained by a few decimeters; however, the precisions start to degrade if the noise exceeds 0.002 m/$\sqrt{\Delta t}$.
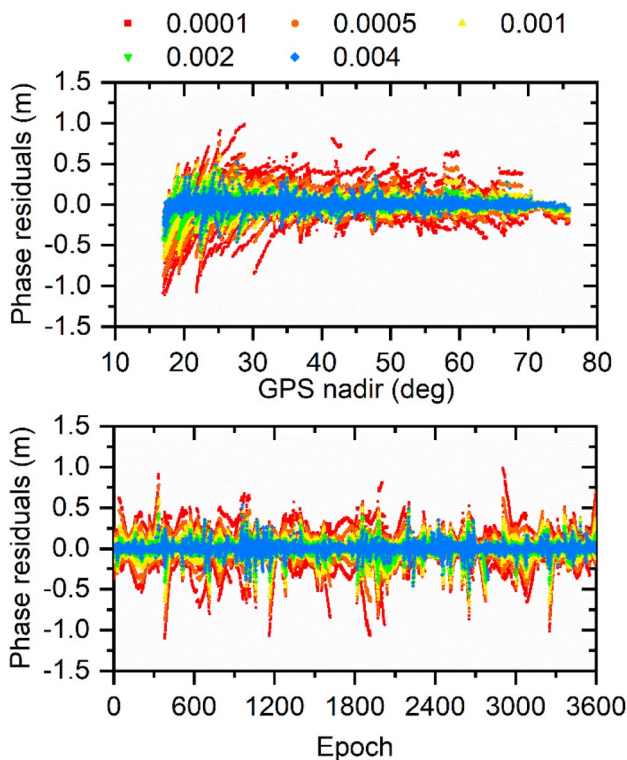

Fig. 9 GPS carrier-phase residuals against GPS nadir angles (top panel) and epoch time (bottom panel). Data on DOY 140/2020 is adopted for illustration
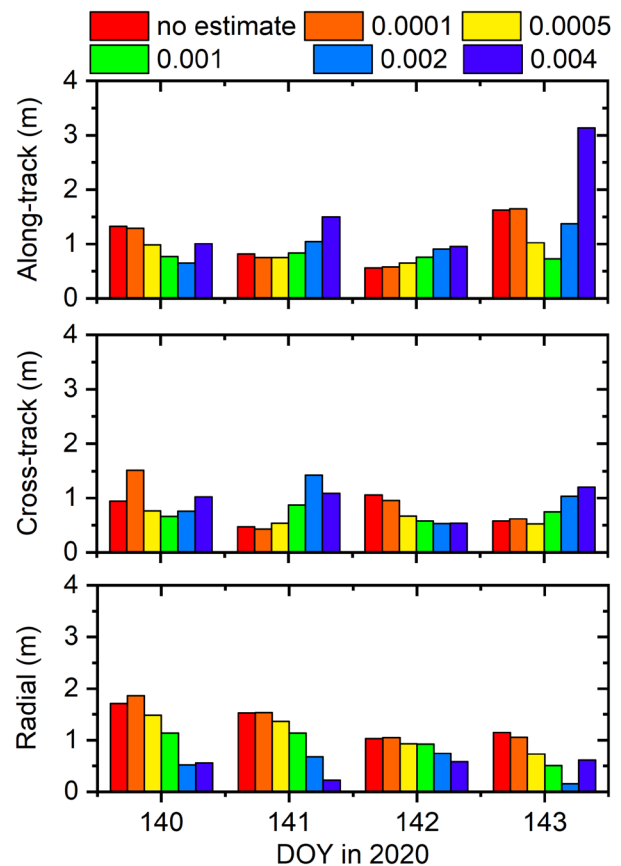

Fig. 10 RMS of TJS-5 OODs in along-track (top panel), cross-track (middle panel), and radial (bottom panel) components. Different colors represent different process noise values assigned to the inconsistency parameter. The baseline OD results (labeled as no estimate) are also illustrated

The average RMS values of the OODs and the post-fit residuals are shown in Table 2. The RMS of carrier-phase residuals indicates impressive decrement from 0.21 m to 0.04 m when the process noise increases, whereas that of code stays around 3.90 m, revealing marginal reduction. The precision of the baseline solution is 1.08 m, 0.76 m, 1.35 m, and 1.95 m in the along-track, cross-track, radial, and 3D components, respectively, comparable to the TJS-2 results (Jiang et al. 2018; Li et al. 2019). Dramatic improvements are found when the process noise is tuned from 0.0005 to 0.002 m/$\sqrt{\Delta t}$, revealing an average orbit precision of around 1.5 m; the radial RMS exhibits steady reductions from 1.23 to 0.53 m. The orbit precision is degraded to 2.02 m when the noise further increases to 0.004 m/$\sqrt{\Delta t}$, at a similar level of the baseline solution. Comparing different test cases, orbit precision is the best when the process noise is 0.001 m/$\sqrt{\Delta t}$, achieving 1.42 m. By applying this constraint, the RMS values in the along-track, cross-track, and radial components are 0.77 m, 0.71 m, and 0.93 m, respectively; and their improvements over the baseline solution are 28.6%, 0.06%, and 31.7%, respectively.

Orbit determination with BDS involved

Considering BDS-3 side-lobe signals show an overall poorer tracking performance than GPS, it is interesting to investigate what OD precision can be achieved with only the BDS observations and to what extent BDS could contribute to GEO OD in the context of GPS and BDS combination. Hence, the TJS-5 OD is performed with the same strategy presented in Table 1 but with different systems; one is only BDS while the other is GPS and BDS combined. The impacts of carrier-code consistencies are also analyzed by comparing the adjusted and the classic carrier-phase model. Thus, four different OD cases are conducted. Their OODs are shown in Fig. 11, while the average RMS values are in Table 3.

With the classic carrier-phase model, the combined OD shows an overall precision below 2.0 m in each component. The radial component shows considerable improvement
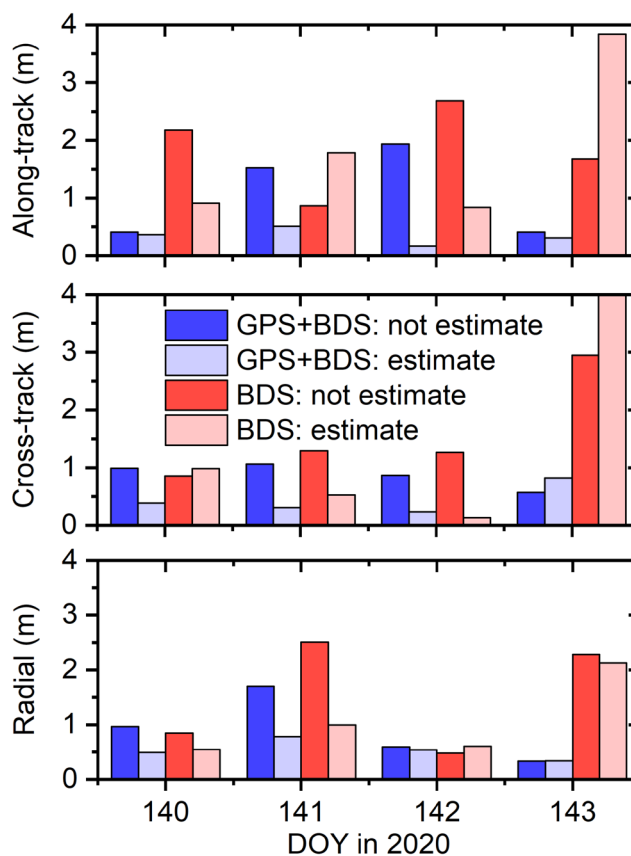

Fig. 11 RMS of TJS-5 OODs in along-track (top panel), cross-track (middle panel), and radial (bottom panel) components. The two blue bars indicate OD results using combined GPS and BDS systems, while the two red bars refer to BDS only. The two light bars represent results with estimating inconsistency parameters (process noise is 0.001 m/$\sqrt{\Delta t}$) while the two dark bars indicate the baseline solutions using the classic model

compared to the GPS OD as the observation geometry is mainly refined along this component; while the other two components are comparable to the GPS OD solution. The average orbit precision is 1.07 m, 0.88 m, 0.90 m, and 1.74 m in the along-track, cross-track, radial, and 3D components, respectively, indicating an orbit precision about 21.4% higher than GPS OD. By estimating the carrier-code

Table 2 TJS-5 OD results with GPS observations using different carrier-phase models

Estimate inconsistency	Process noise (m/$\sqrt{\Delta t}$)	Phase residual (m)	Code residual (m)	Along-track (m)	Cross-track (m)	Radial (m)	3D (m)
×	N/A	0.21	3.95	1.08	0.76	1.35	1.95
√	0.0001	0.20	3.95	1.07	0.88	1.38	2.02
√	0.0005	0.14	3.92	0.85	0.62	1.13	1.57
√	0.001	0.09	3.90	0.77	0.71	0.93	1.42
√	0.002	0.06	3.88	0.99	0.94	0.53	1.51
√	0.004	0.04	3.87	1.65	0.96	0.50	2.02

Table 3 TJS-5 OD results with GPS + BDS and BDS systems. The BDS results labeled with a star in the last two rows indicate the statistics without DOY 144/2020

Systems	Estimate inconsistency	Phase residual (m)	Code residual (m)	Along-track (m)	Cross-track (m)	Radial (m)	3D (m)
GPS + BDS	×	0.22	3.57	1.07	0.88	0.90	1.74
GPS + BDS	√	0.09	3.49	0.34	0.44	0.54	0.82
BDS	×	0.21	2.54	1.85	1.59	1.53	3.14
BDS	√	0.09	2.43	1.85	1.52	1.07	2.71
BDS*	×	0.21	2.57	1.91	1.14	1.28	2.82
BDS*	√	0.09	2.46	1.18	0.55	0.72	1.54

inconsistencies, the orbit errors in all three components are significantly reduced to around 0.5 m, among which the along-track shows the largest improvement. The average RMS values are 0.34 m, 0.44 m, 0.54 m, and 0.82 m in the along-track, cross-track, radial, and 3D components, respectively, revealing improvements compared to the classic model of 68.2%, 50.0%, 40.0%, and 52.9%, respectively. While compared to the GPS OD solution with the adjusted model, the improvements are 60.0%, 38.5%, 41.5%, and 42.2%, respectively, which are attributed to the contribution of BDS.

The BDS solutions indicate overall degraded orbit precisions compared to the GPS OD results, mainly because that the BDS observation number is much fewer, merely half of GPS. The RMS of BDS code residuals is 2.54 m on average, about 35.7% smaller than GPS, while the RMS values of BDS carrier-phase residuals are close to GPS, around 0.21 m and 0.09 m for the classic and adjusted models, respectively. The residual statistics are in line with the observation noise presented in Sect. 3. Attributed to a large observation gap of about 70 min right after the commencement epoch of the OD arc on DOY 144/2020, the RMS of the OODs between DOY 143 and 144/2020 reaches 4.1 m and 6.2 m with the classic and the adjusted model, respectively, which are exceptionally larger than others. The other arcs demonstrate RMS values generally below 3.0 m in each component and show considerable decrements when switching from the classic carrier-phase model to the adjusted one. Considering all OD arcs, the BDS OD precision in the along-track, cross-track, radial, and 3D components is 1.85 m, 1.59 m, 1.53 m, and 3.14 m with the classic carrier-phase model, respectively, while that is 1.85 m, 1.52 m, 1.07 m, and 2.71 m with the adjusted one, respectively, indicating an orbit precision improvement of 13.7% mainly attributed to the radial component. With the OODs between DOY 143 and 144/2020 discarded in statistics, BDS OD precision with the classic model is 1.91 m, 1.14 m, 1.28 m, and 2.82 m in the along-track, cross-track, radial, and 3D components, respectively, while that with the adjusted model

1.18 m, 0.55 m, 0.72 m and 1.54 m, respectively. The orbit precision is improved by about 45.4% with the adjusted model and reaches a similar precision level compared to GPS OD, indicating that the adjusted model applies effectively to the BDS observations as well.

Conclusions

In this study, we collected 5 days of BDS and GPS observations from the Chinese GEO satellite TJS-5 and then utilized them to evaluate the performances of BDS side-lobe signals as well as the BDS contribution to GEO post-dynamic OD.

Due to deficiencies of transmit gain patterns in the side lobes, the tracking capacity for BDS is poorer than GPS. The average GPS satellite number per epoch is 7.8 while BDS is only 4.3. The RMS values of code triple differences are 10.0 m and 5.3 m for GPS and BDS, respectively, while those of carrier-phase are 0.14 cycles and 0.11 cycles, respectively. Significant carrier-code inconsistencies are observed in BDS and GPS observations, which might be due to topside ionospheric refractions or variable hardware delays in different signal lobes.

Post OD is performed with different GNSS system observations. The orbit consistency precision inferred by OODs is 1.95 m with GPS-only observations while that with BDS-only is much worse reaching 3.14 m; this is within expectation as the BDS tracking performance is uncompetitive to GPS. When GPS and BDS are combined, the precision is slightly improved to 1.74 m. Considering the impacts of carrier-code inconsistencies, the carrier-phase observation model is adjusted with the inconsistencies estimated as a random walk process. With this model, the carrier-phase residuals of both GPS and BDS reveal remarkable decrement from 0.21 m to 0.09 m, while the orbital precision is also improved to 1.42 m and 2.71 m with only GPS and only BDS observations, respectively. The GPS and BDS combined OD gain the most impressive orbit precision improvement, achieving 0.82 m.

Our investigations indicate that the BDS side-lobe signal can effectively contribute to improving GEO OD

performances, though its signal availability is degraded due to transmit antenna gains. With the knowledge of BDS transmit gain characters thanks to TJS-5, we would expect TJS-5 and its follow-on missions to further upgrade the tracking strategy as well as the tracking capacity for BDS side-lobe signals. Moreover, the real cause of the GPS and BDS side-lobe carrier-code inconsistencies needs further investigation if more onboard data are gathered.

Data availability All data included in this research are available upon request by contacting the corresponding author.

References

Arnold D, Meindl M, Beutler G, Dach R, Schaer S, Lutz S, Prange L, Sośnica K, Mervart L, Jäggi A (2015) CODE's new solar radiation pressure model for GNSS orbit determination. J Geod 89(8):775–791. https://doi.org/10.1007/s00190-015-0814-4

Ashman B, Bauer FH, Parker J, Donaldson J (2018) GPS operations in high earth orbit: Recent experiences and future opportunities. In: 2018 SpaceOps conference, Marseille, France, May 28–June 1, p 2568. https://doi.org/10.2514/6.2018-2568.

Bauer F, Moreau MC, Dahle-Melsaether ME, Petrofski WP, Stanton BJ, Thomason S, Harris GA, Sena RP, Temple LP (2006) The GPS space service volume. In: Proceedings of ION GNSS 2006, Institute of Navigation, Fort Worth, Texas, USA, September 26–29, p 2503–2514

Bauer FH, Parker JJ, Welch B, Enderle W (2017) Developing a robust, interoperable GNSS space service volume (SSV) for the global space user community. In: Proceedings of ION ITM 2017, Institute of Navigation, Monterey, California, USA, January 30–February 2, pp 132–149

Bizouard C, Lambert S, Gattano C, Becker O, Richard J-Y (2019) The IERS EOP 14C04 solution for Earth orientation parameters consistent with ITRF 2014. J Geod 93(5):621–633. https://doi.org/10.1007/s00190-018-1186-3

Chapel J, Stancliffe D, Bevacqua T, Winkler S, Clapp B, Rood T, Freesland D, Reth A, Early D, Walsh T, Krimchansky A (2017)

In-flight guidance, navigation, and control performance results for the GOES-16 spacecraft. In: 10th international ESA conference on guidance, navigation and control systems, Crowne Plaza Salzburg, Austria, May 29–June 2, pp 1–25

Chapel J, Stancliffe D, Bevacqua T, Winkler S, Clapp B, Rood T, Gaylor D, Freesland D, Krimchansky A (2015) Guidance, navigation, and control performance for the GOES-R spacecraft. CEAS Space J 7(2):87–104. https://doi.org/10.1007/s12567-015-0077-1

Donaldson JE, Parker JJ, Moreau MC, Highsmith DE, Martzen PD (2020) Characterization of on-orbit GPS transmit antenna patterns for space users. Navigation 67(2):411–438. https://doi.org/10.1002/navi.361

Enderle W, Gini F, Boomkamp H, Parker JJ, Ashman BW, Welch BW, Koch M, Sands OS (2018) Space user visibility benefits of the multi-GNSS Space Service Volume: An internationally-coordinated, global and mission-specific analysis. In: Proceedings of ION ITM 2018, Institute of Navigation, Monterey, California, USA, January 30–February 2, pp 132–149

Foerste C, Shako R, Flechtner F, Dahle C, Abrikosov O, Neumayer H, Barthelmes F, Bruinsma SL, Marty J, Balmino G (2011) A new combined global gravity field model including GOCE data from the collaboration of GFZ Potsdam and GRGS Toulouse. In: AGU Fall meeting abstracts, pp 2821

Huang Y, Hu X, Huang C, Yang Q, Jiao W (2009) Precise orbit determination of a maneuvered GEO satellite using CAPS ranging data. Sci China Ser G 52(3):346–352. https://doi.org/10.1007/s11433-009-0052-y

Jiang K, Li M, Wang M, Zhao Q, Li W (2018) TJS-2 geostationary satellite orbit determination using onboard GPS measurements. GPS Solut 22(3):87. https://doi.org/10.1007/s10291-018-0750-x

Li G, Geng J (2019) Characteristics of raw multi-GNSS measurement error from Google Android smart devices. GPS Solut 23(3):90. https://doi.org/10.1007/s10291-019-0885-4

Li W, Li M, Zhao Q, Shi C, Wang M, Fan M, Wang H, Jiang K (2019) Extraction of electron density profiles with geostationary satellite-based GPS side lobe occultation signals. GPS Solut 23(4):110. https://doi.org/10.1007/s10291-019-0903-6

Lin K, Zhan X, Yang R, Shao F, Huang J (2020) BDS Space Service Volume characterizations considering side-lobe signals and 3D antenna pattern. Aerosp Sci Technol 106:106071. https://doi.org/10.1016/j.ast.2020.106071

Lyard F, Lefevre F, Letellier T, Francis O (2006) Modelling the global ocean tides: modern insights from FES2004. Ocean Dyn 56(5):394–415. https://doi.org/10.1007/s10236-006-0086-x

Marquis WA, Reigh DL (2015) The GPS Block IIR and IIR-M broadcast L-band antenna panel: Its pattern and performance. Navigation 62(4):329–347. https://doi.org/10.1002/navi.123

Nicolás-Álvarez J, Broquetas A, Aguasca A (2019) Precise orbit observation techniques for geosynchronous synthetic aperture radar (GEOSAR). In: IGARSS 2019—2019 IEEE international geoscience and remote sensing symposium, Yokohama, Japan, July 28–August 2, pp 8753–8756. https://doi.org/10.1109/IGARSS.2019.8898770

Parker JJ, Valdez JE, Bauer FH, Moreau MC (2016) Use and protection of GPS sidelobe signals for enhanced navigation performance in high Earth orbit. In: 39th annual AAS guidance, navigation and control conference, Breckenridge, Colorado, USA, February 5–10

Petit G, Luzum B, Al. E (2010) IERS conventions (2010). Bureau International des Poids etMesures Sevres (France). https://www.iers.org/IERS/EN/Publications/TechnicalNotes/tn36.html

Ramsey G, Barker L, Chapel J, Winkler S, Frey C, Freesland D, Baltimore P, Krimchansky A (2019) GOES-R series GEO side-lobe capable GPSR post-launch refinements and operational capabilities. In: 42nd annual AAS guidance, navigation and control conference, Breckenridge, Colorado, USA, January 3–February 6.

Rebischung P, Schmid R (2016) IGS14/igs14.atx: a new framework for the IGS products. In: AGU fall meeting, G41A–0998

Su X, Geng T, Li W, Zhao Q, Xie X (2017) Chang'E-5T orbit determination using onboard GPS observations. Sensors 17(6):1260. https://doi.org/10.3390/s17061260

United Nations Office for Outer Space Affairs (2018) The interoperable global navigation satellite systems space service volume. United Nations Office, Vienna. https://digitallibrary.un.org/record/3829212

Wang C, Guo J, Zhao Q, Liu J (2019) Empirically derived model of solar radiation pressure for BeiDou GEO satellites. J Geod 93(6):791–807. https://doi.org/10.1007/S00190-018-1199-Y

Wang M, Shan T, Li M, Liu L, Tao R (2021a) GNSS-based orbit determination method and flight performance for geostationary satellites. J Geod 95(8):1–15. https://doi.org/10.1007/s00190-021-01545-1

Wang M, Shan T, Zhang W, Huan H (2021b) Analysis of BDS/GPS signals' characteristics and navigation accuracy for a geostationary satellite. Remote Sensing 13(10):1967. https://doi.org/10.3390/rs13101967

Wang M, Shan T, Liu L, Huan H, Tao R (2022) On-orbit BDS signals and transmit antenna gain analysis for a geostationary satellite. Adv Space Res 69(7):2711–2723. https://doi.org/10.1016/j.asr.2022.01.022

Winkler S, Ramsey G, Frey C, Chapel J, Chu D, Freesland D, Krimchansky A, Concha M (2017) GPS Receiver On-Orbit Performance for the GOES-R Spacecraft. In: 10th International ESA conference on guidance, navigation and control systems, Salzburg, Austria, May 29–June 2

Winternitz LB, Bamford WA, Price SR, Carpenter JR, Long AC, Farahmand M (2017) Global positioning system navigation above 76,000 KM for NASA'S magnetospheric multiscale mission. Navigation 64(2):289–300. https://doi.org/10.1002/navi.198

Zhao Q, Guo J, Wang C, Lyu Y, Xu X, Yang C, Li J (2022) Precise orbit determination for BDS satellites. Satell Navig 3(1):2. https://doi.org/10.1186/s43020-021-00062-y

Publisher's Note Springer Nature remains neutral with regard to jurisdictional claims in published maps and institutional affiliations.

Kecai Jiang is currently a research assistant at the GNSS Research Center of Wuhan University. He received a Ph.D. at Wuhan University in 2020. His current research mainly focuses on LEO and side lobe signal HEO orbit determination using GNSS.

Min Li received a B.S. degree and Ph.D. degree in Geodesy and Surveying Engineering from Wuhan University, Wuhan, China, in 2005 and 2011, respectively. He is currently a professor at GNSS Research Center of Wuhan University. His main work focuses on GNSS satellite orbit determination and precise point positioning as well as multi-GNSS processing using GPS, GLONASS, BeiDou, and Galileo.

Qile Zhao is a professor at GNSS research center, Wuhan University. He received his doctoral degree from Wuhan University in 2004. He worked as a post-doctoral fellow in 2006–2007 in DEOS, Delft University of Technology, the Netherlands. He is currently a professor at the GNSS Research Center of Wuhan University, and his current research interests are GNSS/LEO precise orbit determination and high-precision positioning with GPS, GLONASS, BeiDou, and Galileo.

Wenwen Li is a research assistant at GNSS Research Center, Wuhan University. He obtained his doctoral degree at Wuhan University in 2019. His main research interests include LEO/HEO satellite onboard GNSS data analysis and orbit determination, and it applications in atmosphere sensing.

Meng Wang is a senior engineer of Beijing Institute of Satellite Information Engineering Company. His research interests include high-altitude spacecraft navigation, multi-GNSS receiver design, and weak signal processing.

Chuang Shi is a professor at Beihang University. He graduated from Wuhan University and obtained his PhD degree in 1998. His research interests include network adjustment, precise orbit determination of GNSS satellites and LEOs and real-time precise point positioning.

Caijun Xu received his Ph.D. in Geodesy at Wuhan University. He is the specially appointed professor of the Cheung Kong Scholars Program, and vice dean of Geodesy and Geomatics, Wuhan University. He is a member of the Sub-Committee of Applications of Satellite and Airborne Imaging Systems of International Association of Geodesy (IAG). His research interests are Geodesy and Seismology.